WILEY | Hindawi

Research Article

Angular Stability Enhancement Using Phase Compensation Method for Frequency Selective Surface Design

Yiwei Chen [ID],[1] **Yang Yang** [ID],[1] **Xiaoxiang He** [ID],[1] **Xiaohui Yu** [ID],[1] and **Wenwu Zhang** [ID][2]

[1]*College of Electronic and Information Engineering, Nanjing University of Aeronautics and Astronautics, Nanjing, China*
[2]*Research Institute For SPECIAL Structures of Aeronautical Composites AVIC, Jinan, China*

Correspondence should be addressed to Xiaoxiang He; eexxhe@nuaa.edu.cn

This study introduces a novel phase compensation-based, asymmetric frequency selective surface (FSS). Aimed at enhancing angular stability, the phase compensation method utilizes the reflected phase gradient changes generated by two FSSs at large grazing angles. The ultimate improvement in angular stability comes from unit amalgamation to achieve phase complementarity, effectively dealing with the phase shift of incident waves caused by large grazing angles. Based on this principle, the asymmetric FSS structure is built with 3 components: a Minkowski fractal cell, a bent-line square-loop cell, and a thin square-loop parasitic cell. Simulation results show the structure demonstrates a 0 relative shift of resonant frequency within an incidence range of 0-80° under transverse electric (TE) polarization. However, it exhibits a maximum relative shift of 5.12% in resonant frequency at an 80° incidence under transverse magnetic (TM) polarization. Compared with E_1 and E_2 units, this structure significantly reduces frequency deviation—by 100% at 80° incidence under TE polarization and by 80.12% and 83.26% compared with E_1 and E_2 units under TM polarization. Finally, the proposed FSS model was fabricated and processed, with measured data basically aligning with the simulated results.

1. Introduction

Frequency selective surface (FSS) is a periodic array structure with the capacity to manipulate the transmission or reflection of electromagnetic waves. These arrays usually consist of single or multiple resonant cells composed of metal patches arranged in a specific pattern. Given its practical applications, FSS often encounters a broad range of incident wave angles, demanding a consistently performing structure across these varying angles. Consequently, exploration of FSS angular stability becomes critical.

Prevailing strategies to tackle angular stability include the adoption of compact cell arrangement with miniaturization attributes to postpone the appearance of the gate flap. Designs such as folded cross-finger [1–3], multilayer [4–9], and fractal [10] help to achieve the angular insensitivity of FSS. Certain methods like 2.5-dimensional FSS [11, 12] and 3-dimensional FSS [13, 14] have also been employed for improved angular stability. These approaches have proven effective for ensuring good angular stability within a 0-60° range. This work intro-

duces a phase compensation method for FSS design, thereby augmenting angular stability up to 0-80°. This allows for a more flexible deflection of the refracted beam wave vector, expanding the possibilities for enhancing angle stability.

To validate this method, a $6 \times 12 \times 0.5$ mm FSS comprising a Minkowski fractal cell, a bent-line square-loop cell, and a thin square-loop parasitic cell is presented. This novel FSS demonstrates resonant angular stability of up to 80° for both transverse electric (TE) and transverse magnetic (TM) modes. The paper is further organized as follows: Section 2 presents the FSS unit cell's design and characterization. Section 3 delves into an investigation of angular stability. The FSS prototype's fabrication and measured results are reported in Section 4.

2. Structure and Operating Principles

2.1. Generalized Snell Theorem. When the electromagnetic wave emitted from the feed source interacts with the array surface at an oblique incidence, as shown in Figure 1, each
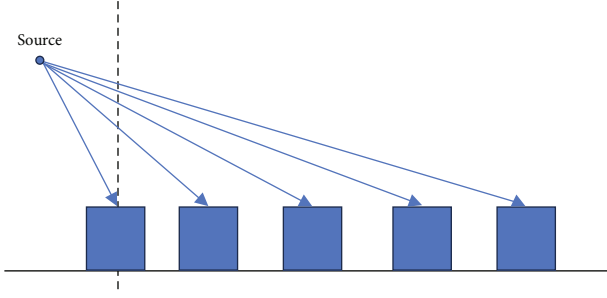
FIGURE 1: Schematic diagram of electromagnetic waves obliquely interacting with periodic structure.

FIGURE 2: Schematic diagram of generalized Snell theorem.

resulting return signal will form a distinct phase difference through each propagation path.

Assuming the electromagnetic wave originates from point A, the electromagnetic wave ranges of ABD and ACD are infinitely close to each other. Therefore, when a wave traverses these two optical ranges, an identical phase gradient can be produced, yielding a phase difference of 0 in both cases. In Figure 2, the phase accumulation for these two wave ranges is as follows:

$$\phi_{ABD} = \phi + \phi_{AB} + \phi_{BC'} + \phi_{C'D},$$
$$\phi_{ACD} = \phi + \phi_{AB'} + \phi_{B'C} + \phi_{CD} + d\phi, \qquad (1)$$

where ϕ is the phase of the incident wave.

Assuming $AB \approx AB'$, $CD \approx C'D$ is obtained as follows:

$$\phi + \phi_{BC'} = \phi + \phi_{B'C} + d\phi. \qquad (2)$$

Let $BC = dx$, then $B'C = k_0 n_i \sin \theta_i dx_i$. Assuming $\angle DCC' = 90°$, $\angle BCC' = \angle DCE = \theta_i$, thus $BC' = k_0 n_i \sin \theta_r dx_i$, substituting these into

$$k_0 n_i \sin \theta_r dx + \phi = k_0 n_i \sin \theta_i dx + \phi + d\phi. \qquad (3)$$

Similarly, Equation (4) can be obtained as follows:

$$k_0 n_t \sin \theta_t dx + \phi = k_0 n_i \sin \theta_i dx + \phi + d\phi. \qquad (4)$$

Upon sorting the above equation and removing similar terms, the generalized Snell reflection and refraction theorem is obtained as follows:

$$\sin \theta_r = \sin \theta_i + \frac{1}{k_0 n_i} \frac{d\phi}{dx}, \qquad (5)$$

$$n_t \sin \theta_t = n_i \sin \theta_i + \frac{1}{k_0} \frac{d\phi}{dx}. \qquad (6)$$

2.2. Principle of Anomalous Refraction. The generalized Snell theorem introduces a phase gradient $d\emptyset/dx$ to achieve relative quiescence of the overall phase shift, culminating in anomalous refraction phenomena.
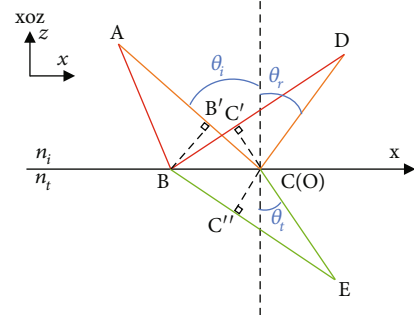
From Equation (6), a relationship can be derived between the refraction angle, the incident angle, and the phase compensation angle on the dividing surface:

$$\theta_t = \sin^{-1}\left(\frac{1}{n_t} \sin \theta_i + \frac{1}{n_t} \frac{1}{k_0} \frac{d\phi}{dx} \right), \qquad (7)$$

where the wave vector $k_0 = 2\pi/\lambda$ and the refractive index $n_i = 1$ in free space. Since the domain of definition for $y = \sin^{-1}x$ is $[-1, 1]$, the equation must satisfy

$$\left| \frac{1}{n_t} \sin \theta_i + \frac{1}{n_t} \frac{1}{k_0} \frac{d\phi}{dx} \right| \leq 1 \qquad (8)$$

for the refraction angle θ_t to have a solution. Specifically, this circumstance signifies the onset of anomalous refraction.

The above equation derives the quantitative correlation between the refraction and the transmission phase difference between adjacent cells of FSS exhibiting anomalous refraction. By rationalizing the cell size p and the phase difference $d\emptyset/dx$ between adjacent cells, scattered waves can be steered more towards the normal direction. This is close to the transmission performance at normal incidence and it ultimately improves the angular stability of the structure.

2.3. Description of the Proposed FSS Structure. Based on this theory, the one-dimensionally distributed FSS structure comprises two units having specific transmission phases and transmission amplitudes. This is used to compensate for the phase difference, which is formed when waves propagate through different paths to the array surface. The transmitted wave undergoes anomalous refraction so that the beam refraction direction is biased towards the normal direction, thereby improving angular stability. Therefore, as shown in Figure 3, the design of FSS is meticulously structured as follows: E_1 is the Minkowski fractal FSS and E_2 is the bending line square ring FSS. Both FSS structures are mounted on an FR-4 sheet measuring $6 \times 12 \times 0.5$ mm. To bolster stability and optimize performance, a parasitic patch is strategically employed, surrounding the main radiating patch. This parasitic patch, designed in the form of a box cell with an inner diameter of 0.05 mm, contributes significantly to enhancing the overall electromagnetic coupling effect within the FSS configuration. A crucial objective of
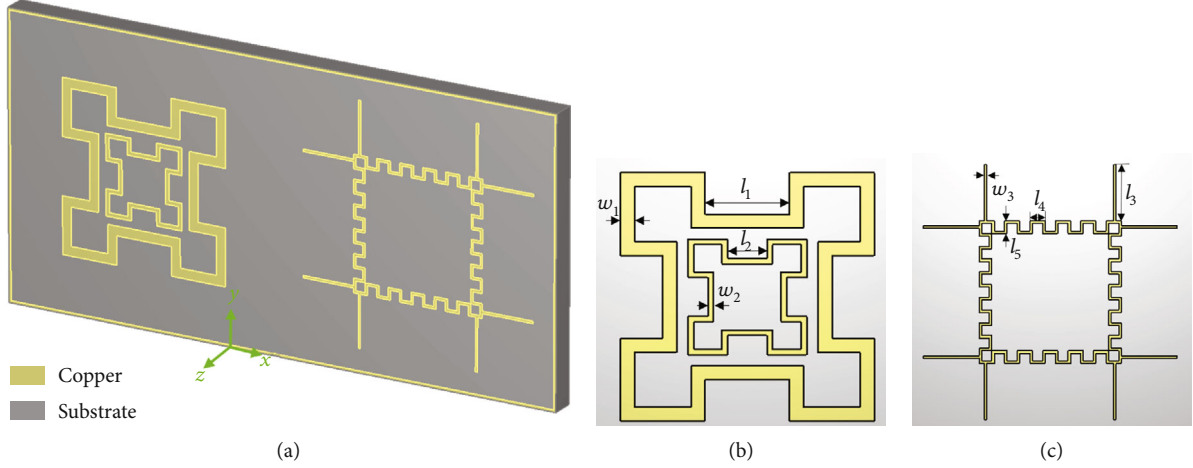
FIGURE 3: Unit cell geometry of (a) proposed hybrid FSS. (b) Main radiation patch E_1. (c) Parasitic patch E_2.

arranging the box cell is to avoid the appearance of additional resonance points within the low-frequency band, which could affect the original filtering characteristics. Its detailed structure and dimension parameters are presented in Table 1.

The resonant performance of E_1 and E_2 units are similar, along with different resonant frequency points. Specifically, for frequency $f = 10$ GHz and period size $p = 12$ mm, $d\phi$ is determined in the range of (-180°, 2.3°) at an incident angle of 80° by substituting into Equation (8).

The phase difference between E_1 and E_2 is depicted in Figure 4, revealing that phase compensation is not observed within the nonresonant band. However, a significant transmission phase difference between E_1 and E_2 manifests within the interval of the resonant frequency. The designed phase difference shown in Figure 4(e) satisfying condition for achieving anomalous refraction allows for the emergence of anomalous scattering behavior in FSS configuration.

3. Simulation Results and Discussions

3.1. Angular Stability Analysis. As evidenced in Figures 5(a)–5(c), the reflection coefficients of E_1, E_2, and the hybrid FSS are presented by the microwave simulation software CST.

In TE mode, the resonant frequencies of E_1 were observed at 10.05 and 10.16 GHz at 0° and 80° incident angles, respectively. This accounts for a relative frequency shift of 1.09% from the center frequency at 80° compared to the frequency at normal incidence. The resonant frequencies of E_2 at 0° and 80° incident angles were 9.06 and 9.04 GHz, respectively, yielding a relative frequency shift of 0.33%. Additionally, the hybrid cell's resonant frequency points remain consistent at 7.108 GHz at both 0° and 80° incident angles, exhibiting no shift.

In TM mode, the resonant frequency points of E_1 at 0° and 80° incident angles stood at 10.08 and 12.67 GHz, respectively, indicating a relative frequency shift of 25.69%. The resonant frequency points of E_2 at 0° and 80° incident angles were 9.11 and 11.79 GHz, respectively, yielding a relative frequency shift of 29.42%. Conversely, the resonant

TABLE 1: Parameters of proposed FSS.

Parameter	L_1	L_2	L_3	L_4	L_5
Value	1.2 mm	0.56 mm	1.1 mm	0.3 mm	0.25 mm
Parameter	w_1	w_2	w_3	h	
Value	0.2 mm	0.08 mm	0.05 mm	0.5 mm	

frequency points of the hybrid unit at 0° and 80° incident angles were 9.46 and 9.94 GHz, respectively, yielding a relative frequency shift of 5.07%.

The resonant frequency shifts to each cell at each angle of incidence compared to the normal incidence in both TE and TM modes are depicted in Figures 5(d) and 5(e), respectively. The figure demonstrates a significant decrease in the resonant frequency shift for each polarization and incident angle when the cells were combined.

Figures 6(a)–6(c) display the transmission coefficient of E_1, E_2, and the hybrid FSS. Based on this, the insertion loss of E_1 and the hybrid FSS is given in Table 2. In TE mode, the insertion loss of the hybrid FSS at 0° and 80° incident angles was reduced by 0.1 dB and 0.53 dB, respectively, compared with E_1. However, the insertion loss had no improvement in TM mode. These results indicated that the insertion loss of the FSS can be improved by using phase combination units.

Under an incident angle of 80°, the passband bandwidth (transmission coefficient > −3 dB) for E_1 was 1.3 GHz, for E_2 was 1.1 GHz, and for the hybrid FSS was 2.2 GHz in TE mode. Alternatively, the passband bandwidths of E_1 and E_2 were both 11 GHz, while the hybrid cell exhibited an overall bandwidth of 10.8 GHz in TM mode. For an 80° incident angle under TE polarization, the passband bandwidth of the hybrid cell increased by 69.2% and 100% compared to E_1 and E_2, respectively. Conversely, for an 80° incident angle in TM mode, the bandwidth of the hybrid cell decreased by 0.2 GHz compared to E_1 and E_2. This can be attributed to the coupling effect generated by the cell combination, which shifts the resonant frequency point of the reflection from a higher to a lower frequency.
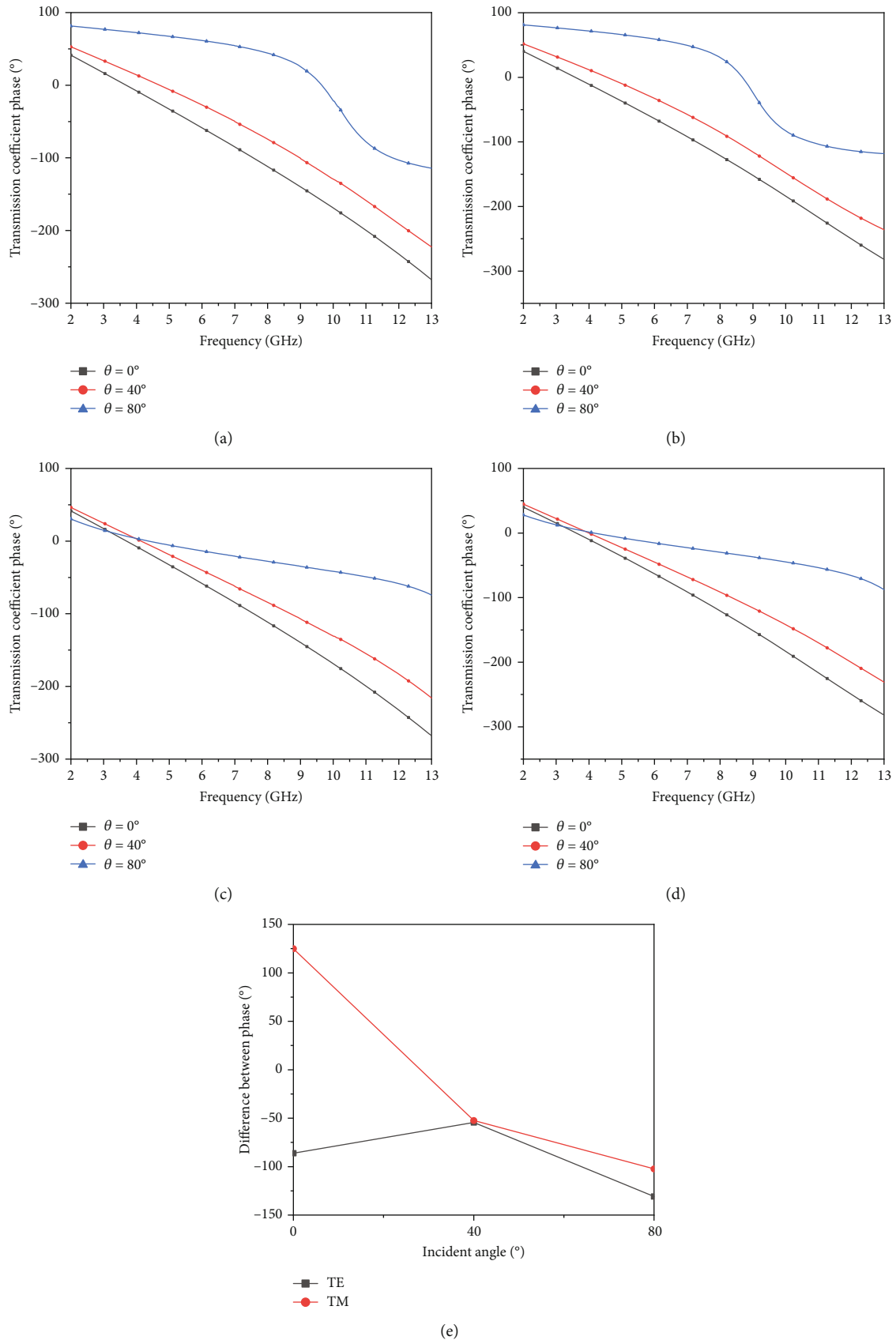
(a)

(b)

(c)

(d)

(e)

FIGURE 4: Phase characteristics in TE mode. (a) Phase angle of E_1. (b) Phase angle of E_2. Phase characteristics in TM mode. (c) Phase angle of E_1. (d) Phase angle of E_2. Phase Characteristics in TE and TM modes. (e) Phase difference between E_1 and E_2.
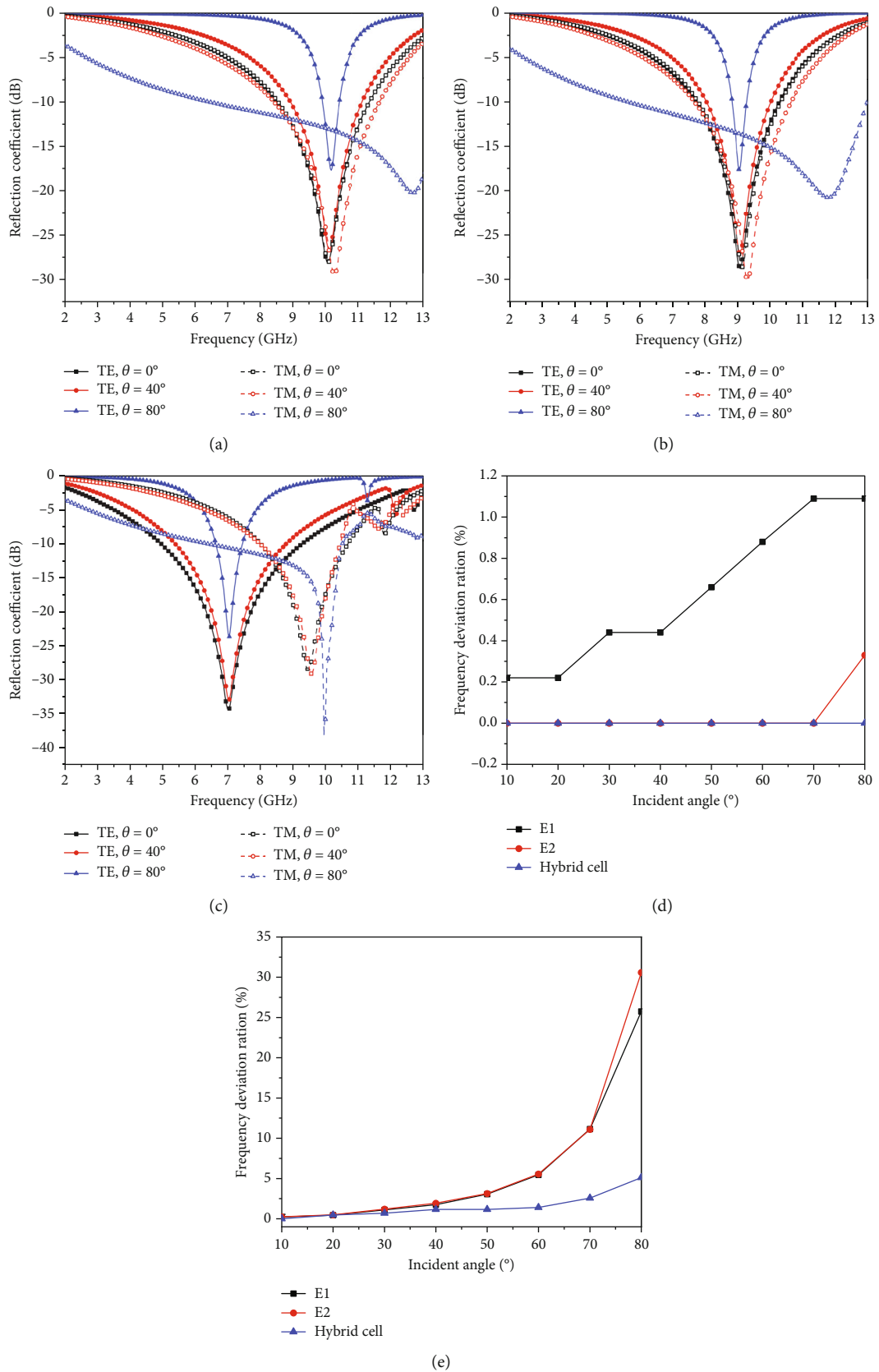
FIGURE 5: Reflection characteristics of hybrid FSS in TE and TM incidence from 0° to 80°. (a) Reflection coefficient of E_1. (b) Reflection coefficient of E_2. (c) Reflection coefficient of the hybrid FSS. (d) Frequency deviation ratio of the hybrid FSS in TE mode. (e) Frequency deviation ratio of the hybrid FSS in TM mode.
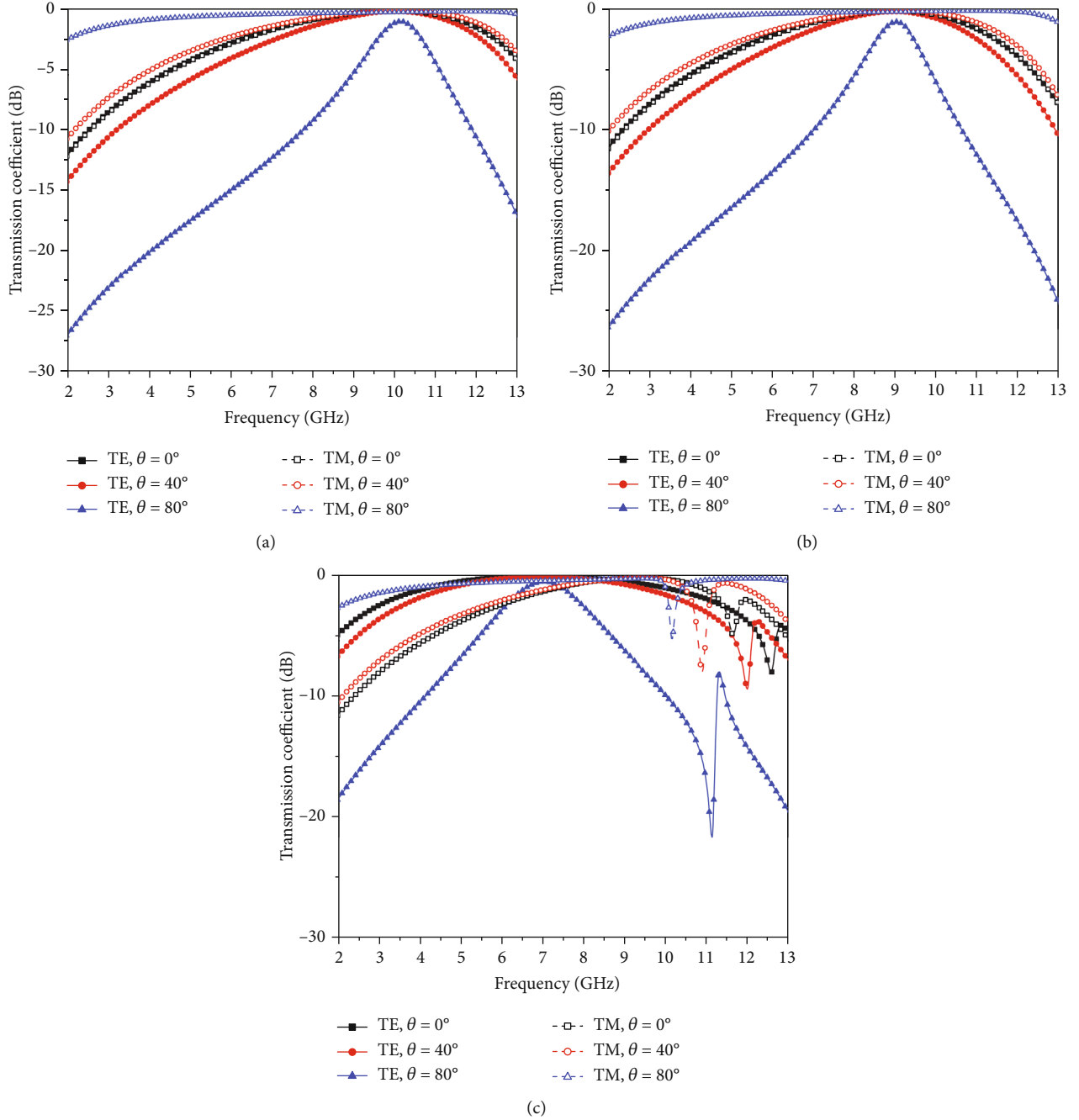
(a)

(b)

(c)

FIGURE 6: Transmission coefficient of hybrid FSS in TE and TM incidence from 0° to 80°: (a) E_1, (b) E_2, and (c) hybrid FSS.

TABLE 2: Insertion loss comparison between E_1 and hybrid FSS.

		0°	40°	80°
TE	E_1	-0.19 dB	-0.25 dB	-1.06 dB
	Hybrid FSS	-0.09 dB	-0.12 dB	-0.53 dB
TM	E_1	-0.19 dB	-0.17 dB	-0.23 dB
	Hybrid FSS	-0.18 dB	-0.19 dB	-0.25 dB

3.2. Abnormal Refraction Effect Analysis. Figure 7 presents the far-field 3D scattering direction diagram. E_1, E_2, and the hybrid unit all produced a potent scattered beam in the direction when $\theta_t = 0°$. At an incident angle of 80°, the original scattered beam of E_1 shifted to $\theta = 66 \pm 31.5°$, that of E_2 shifted to $\theta = 74 \pm 31.5°$, and that of the hybrid FSS shifted to $\theta_t = 56 \pm 17.5°$.

The simulation outcomes indicate that, with increasing incident angle, the beam energy in the perpendicular direction of E_1 and E_2 weakened, while the primary beam energy shifted towards the traditional refraction direction. On the other hand, the hybrid FSS gradually shifted its primary
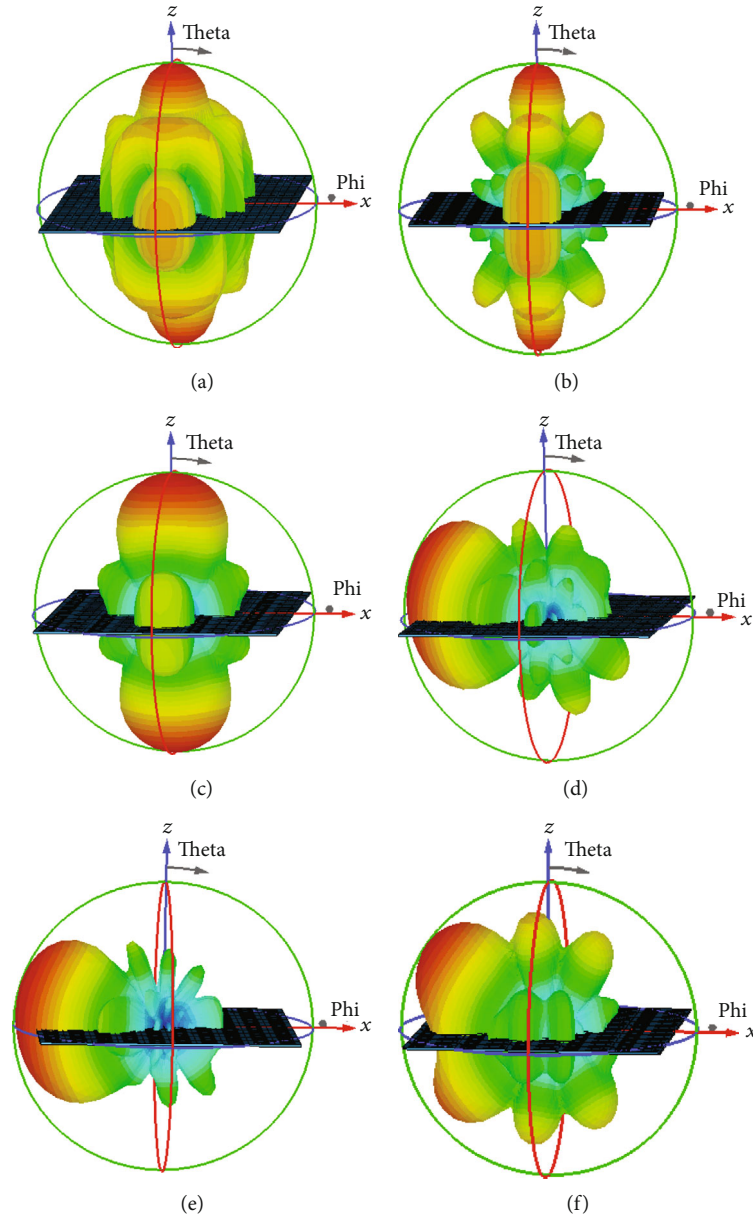
FIGURE 7: Far-field 3D scattering direction diagram of (a) E_1 at 0°, (b) E_2 at 0°, (c) hybrid FSS at 0°, (d) E_1 at 80°, (e) E_2 at 80°, and (f) hybrid FSS at 80°.

beam energy, but the offset angle remained smaller than that of the conventional refraction direction. These results additionally supported the observation that the hybrid FSS achieved anomalous refraction.
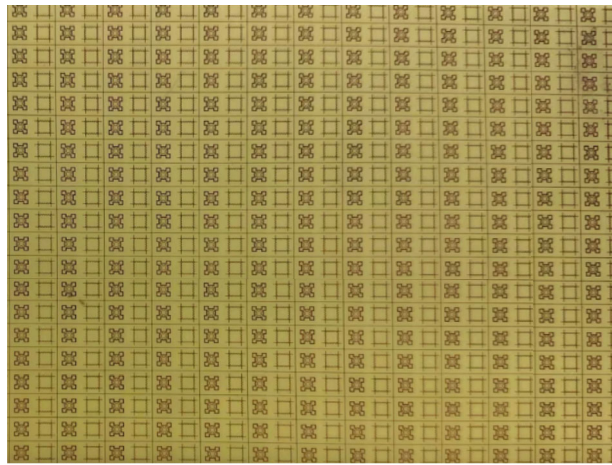
4. Fabrication and Measurement

A physical sample of the hybrid FSS, employing the phase compensation principle, was tested in a microwave anechoic chamber. The sample consists of a 40×40 unit arrangement, and the testing setup uses an Agilent N5230C vector network analyzer alongside two diagonal horn antennas. The antennas are arranged on opposite sides of the sample, serving as transmitting and receiving

devices, as depicted in Figure 8. The testing aims to evaluate the reflection coefficient at incident angles of 0° and 80° in both TE and TM modes.

Figure 9 shows the measured curve and the simulated curve of the hybrid FSS's reflection coefficient, with the electromagnetic wave incident at 0° and 80° under both TE and TM polarizations. The slight shift in the measured results' central resonance frequency point of less than 0.43 GHz may be attributed to fabrication discrepancies and variability in the dielectric plate material. This discrepancy may also be due to the measurement being carried out on a finite array, while the simulation considered an infinite array through unit cell boundary conditions. The potential impact of fabrication tolerances, due to the unit cell's
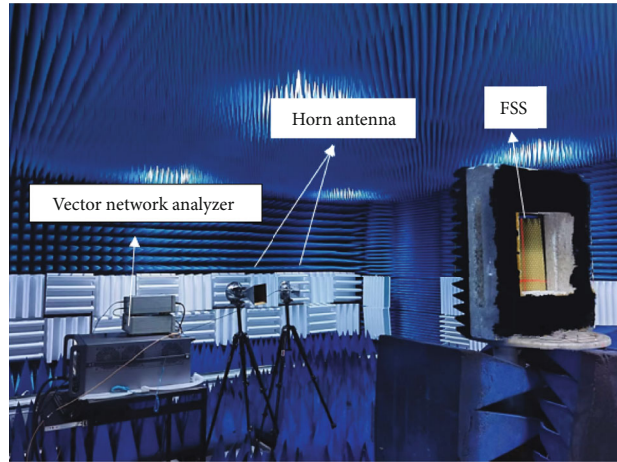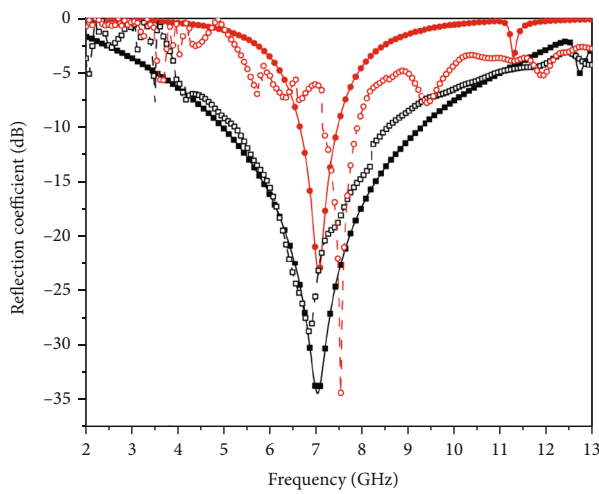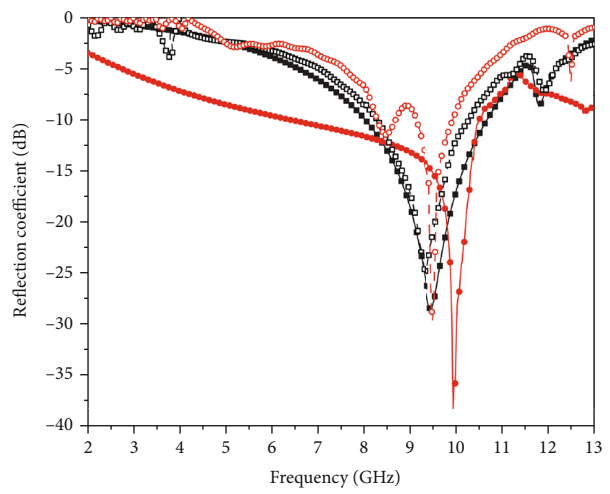
(a)

(b)

Figure 8: Fabrication and measurement of the simplified FSS prototype. (a) Measurement setup. (b) Front view of FSS prototype to be tested.

(a)

(b)

Figure 9: Comparison of measured and simulated reflection coefficients of the hybrid FSS as a function of incident angle. (a) TE mode at $0°$ and $80°$. (b) TM mode at $0°$ and $80°$.

minute dimensions, and the environmental conditions in the anechoic chamber also cannot be overlooked as contributing factors to this deviation.

The collected results, spanning a range from 2 to 13 GHz, reveal some objective observations. Objectively, the wave impedance change of FSS with the angle in both TE and TM polarizations yields contrasting results. In TE mode, the resonant frequency point shifted towards a higher frequency by 0.41 GHz. Conversely, in TM mode at 80° incidence, the resonant frequency point shifted to the lower frequency by 0.43 GHz. The relative drift of the resonant frequency point at an 80° incidence, compared to normal incidence, is 10.6% in TE mode and 2.1% in TM mode.

5. Conclusion

This study presents the design of a hybrid FSS that amalgamates miniaturized FSS cells. This configuration mitigates the emergence of the grating lobes through phase compensation. The relative offset of the hybrid unit's reflected resonant frequency point in TE mode is 0 across an incident angle range of 0-80°. In TM mode, this offset sees a reduction of 80.12% and 83.26% compared to E_1 and E_2 units, respectively. These results suggest that the hybrid unit significantly affected the resonant frequency shift of FSS at large incident angles. The measured data aligned well with the simulation results.

Data Availability

The simulation and testing data used to support the findings of this study are included within the article.

Conflicts of Interest

The authors declare that they have no conflicts of interest.

References

[1] R. Sivasamy and M. Kanagasabai, "A novel dual-band angular independent FSS with closely spaced frequency response," *IEEE Microwave and Wireless Components Letters*, vol. 25, no. 5, pp. 298–300, 2015.

[2] T. Cheng, Z. Jia, T. Hong, W. Jiang, and S. Gong, "Dual-band frequency selective surface with compact dimension and low frequency ratio," *IEEE Access*, vol. 8, pp. 185399–185404, 2020.

[3] A. Vallecchi and A. G. Schuchinsky, "Entwined planar spirals for artificial surfaces," *IEEE Antennas and Wireless Propagation Letters*, vol. 9, pp. 994–997, 2010.

[4] G. Shah, Q. Cao, Z. U. Abidin, and Z. Rafique, "A hybrid element triband frequency selective surface with high angular stability and polarization insensitivity," *IEEE Transactions on Electromagnetic Compatibility*, vol. 62, no. 6, pp. 2759–2764, 2020.

[5] X. Ma, Y. Liu, G. Wan, and A. Pan, "Angularly stable frequency-selective surface using shifted double-sided screens," *IEEE Antennas and Wireless Propagation Letters*, vol. 19, no. 7, pp. 1192–1196, 2020.

[6] N. Liu, X. Sheng, C. Zhang, and D. Guo, "Design of frequency selective surface structure with high angular stability for radome application," *IEEE Antennas and Wireless Propagation Letters*, vol. 17, no. 1, pp. 138–141, 2018.

[7] H.-H. Chou and G.-J. Ke, "Narrow bandpass frequency selective surface with high level of angular stability atKa-band," *IEEE Microwave and Wireless Components Letters*, vol. 31, no. 4, pp. 361–364, 2021.

[8] X. Liu, Q. Wang, W. Zhang, M. Jin, and M. Bai, "On the improvement of angular stability of the 2nd-order miniaturized FSS structure," *IEEE Antennas and Wireless Propagation Letters*, vol. 15, pp. 826–829, 2016.

[9] D. Yang, H. Zhai, R. Qi, and K. Xue, "A reconfigurable frequency selective surface with wide reconfigurable passband and angular stability property," *Microwave and Optical Technology Letters*, vol. 62, no. 6, pp. 2189–2194, 2020.

[10] D. J. Kern, D. H. Werner, A. Monorchio, L. Lanuzza, and M. J. Wilhelm, "The design synthesis of multiband artificial magnetic conductors using high impedance frequency selective surfaces," *IEEE Transactions on Antennas and Propagation*, vol. 53, no. 1, pp. 8–17, 2005.

[11] D. Li, T.-W. Li, E.-P. Li, and Y.-J. Zhang, "A 2.5-D angularly stable frequency selective surface using via-based structure for 5G EMI shielding," *IEEE Transactions on Electromagnetic Compatibility*, vol. 60, no. 3, pp. 768–775, 2018.

[12] T. Li, D. Li, P. Qin et al., "A novel miniaturized strong-coupled FSS structure with excellent angular stability," *IEEE Transactions on Electromagnetic Compatibility*, vol. 63, no. 1, pp. 38–45, 2021.

[13] S. Ghosh and S. Lim, "A miniaturized bandpass frequency selective surface exploiting three-dimensional printing technique," *IEEE Antennas and Wireless Propagation Letters*, vol. 18, no. 7, pp. 1322–1326, 2019.

[14] D. Hu, H. Zhai, L. Liu, J. Shi, and Z. Nie, "A new miniaturized frequency selective surface designed for Ku-band absorption and low-frequency bandpass," *Microwave and Optical Technology Letters*, vol. 62, no. 1, pp. 315–321, 2020.